

Vorticity transfer in a leading-edge vortex due to controlled spanwise bending

Kun Jia ¹, Tyler Scofield ², Mingjun Wei ¹ and Samik Bhattacharya^{2,*}

¹*Department of Mechanical and Nuclear Engineering, Kansas State University,
Manhattan, Kansas 66506, USA*

²*Mechanical and Aerospace Engineering Department, University of Central Florida,
Orlando, Florida 32816, USA*



(Received 15 January 2020; accepted 9 February 2021; published 25 February 2021)

Many natural flyers and swimmers routinely flex their lifting or propulsive surfaces to control the leading-edge vortex (LEV) that forms on the suction side during maneuvering at a high angle of attack. In this paper, we studied the effect of a similar bending on the vortex dynamics of a flat-plate airfoil of aspect ratio 3 (chord 5 cm) and held at an angle of attack of 30°. This flat plate is accelerated from rest to a Reynolds number of 2400, while being dynamically bent along the span in a controlled manner with a bending ratio of 0.65 and a maximum bending angle of 30°. We investigated the effect of such spanwise bending on the resultant vorticity transfer via both experiments and numerical simulation. It shows that a dynamic spanwise bending induces a change in the effective shear layer velocity along the span's bent part and creates spanwise vorticity convection. As a result, the growth of circulation in the LEV gets delayed along the bent part, and the final circulation is smaller than the no-bending case.

DOI: [10.1103/PhysRevFluids.6.024703](https://doi.org/10.1103/PhysRevFluids.6.024703)

I. INTRODUCTION

A vast majority of animals bend their fins or wings to generate thrust, and Lucas *et al.* [1] have shown that such bending patterns follow surprisingly similar kinematics across animal taxa. During high angle of attack maneuvers in the low-Reynolds-number regime, the unsteady forces are mostly caused by vortices formed due to massive flow separation. Natural flyers and swimmers are deft at manipulating these unsteady aerodynamic and hydrodynamic forces with the help of wing morphing. Such capability requires precise control of the vortices that form during an unsteady maneuver. Unfortunately, engineering systems are far behind natural flyers in this respect, as the effect of dynamic shape change on the unsteady fluid mechanics is still being explored. The present paper makes an effort to reduce this knowledge gap by investigating the effect of dynamic spanwise bending on the resultant vorticity transfer mechanisms. We elucidate the vortex dynamics of a dynamically bent flat plate and detail how a simple spanwise bending can alter the vorticity distribution on the flat plate.

In the low-Reynolds-number (low-Re) regime, many high angle of attack maneuvers result in the formation of vortices on the wing leading or trailing edges. For example, during acceleration from rest at a relatively high angle of attack, the laminar boundary layer separates and rolls up to form a leading-edge vortex (LEV) [2]. This LEV gradually grows in size, rolls over, and gets shed in the wake [3]. The formation of the LEV depends on the supply of vorticity by the separated shear layer. As long as this supply continues, the LEV grows in size. However, there is a limit up to which this growth can continue. Dabiri [4] denoted this limit using the concept of optimal formation time. After

*Corresponding author: samik.bhattacharya@ucf.edu

the optimal formation time is reached, the vortex pinches and gets shed in the wake. The concept of formation time alludes to a threshold vorticity level over which the core of a LEV is no longer able to sustain itself and cuts off the supply of circulation from the leading edge.

Now, we want to adjust the process so that this LEV stays on the suction surface longer because it will subsequently generate lift and last longer. Insects achieve this goal by rapidly flapping their wing and utilizing rotational acceleration to delay the pinch-off process [5]. For other applications, one must devise a way to constantly remove vorticity from the core to increase the LEV stability. Ellington *et al.* [6] argued that spanwise flow could be effective in increasing the LEV stability by removing vorticity from the LEV core to the tip vortices. Wong and Rival [7] showed that spanwise vorticity convection and vortex stretching are effective in controlling the LEV growth. Using a topological argument, Rival *et al.* [8] showed that only vortices smaller than the wing's chord could stay stably attached to the wing.

An important aspect of studying the effect of surface deformation of a wing on the vortex dynamics is the role of flexibility [9]. Consequently, many researchers have studied the effect of passive flexibility in flapping propulsion [10–13]. It is known that insects' wings are passively flexible due to the absence of internal muscles [14]. Heathcote *et al.* [15] studied the effect of passive flexibility of a heaving plate on the thrust produced and found that spanwise flexibility was beneficial for Strouhal numbers (St) between 0.2 and 0.4. This is the range of St that can be found in natural flyers across different animal taxa. In fact, for natural flyers and swimmers, Lucas *et al.* [1] found that an optimal bending pattern exists with a mean bending ratio of 0.65 and a mean bending angle of 26.5° .

Unlike insects, many natural flyers and swimmers possess internal muscle tissues and can control the directional flexibility of their wings or fins to gain propulsive benefits. This ability enables them to attain a high degree of maneuverability and control. Such controls can be effected with a complex deformation pattern of the wing surface, such as a combined bending and twisting resulting in spanwise variation of the LEV. The effect of active bending or twisting has received less attention than passive flexing, probably due to the difficulty of making actuated models. Liu and Bose [16] studied the propulsive performance of oscillating foils with spanwise flexibility using a time-domain panel method. They showed that propulsive efficiency could be improved by controlling the phase of the spanwise flexibility relative to other motion parameters. In-phase motions resulted in significant improvement of thrust. Recently, Wong and Rival [17] showed that the relative phase of the bending with the main motion would determine the flow field over the wing for an undulating propulsor. If the tip region of the wing is being bent along the direction of the mean flow, the relative velocity will decrease and the supply of circulation will decrease. This will result in a spanwise variation in the structure of the LEV.

With the rapid development of smart materials, active morphing is now a reality. In low-Reynolds-number applications, where the convective velocities are much smaller, such surface deformations can effectively control the flow's vortex dynamics over a surface. In the present research, we investigate similar fluid physics over a flat-plate wing that undergoes a gradual spanwise bending when accelerated from rest to a Re of 2400. We conducted experiments and direct numerical simulations to investigate the changes in the vortex dynamics of the flat plate during such an unsteady flow.

II. MATERIALS AND METHODS

A. Wing model and kinematics

We used a flat plate of chord 5 cm, span 15 cm (aspect ratio 3), and thickness 4 mm for this work. This plate was three-dimensional (3D) printed from nylon plastic, and it had a rounded leading edge and a sharpened trailing edge to ensure the Kutta condition. Two prebent rods were inserted into the plate through two curved grooves [Fig. 1(a)]. These rods were bent on one end to mimic the desired curvature of the tip. As the rods rotated, the plate acted as a skin following the contour with

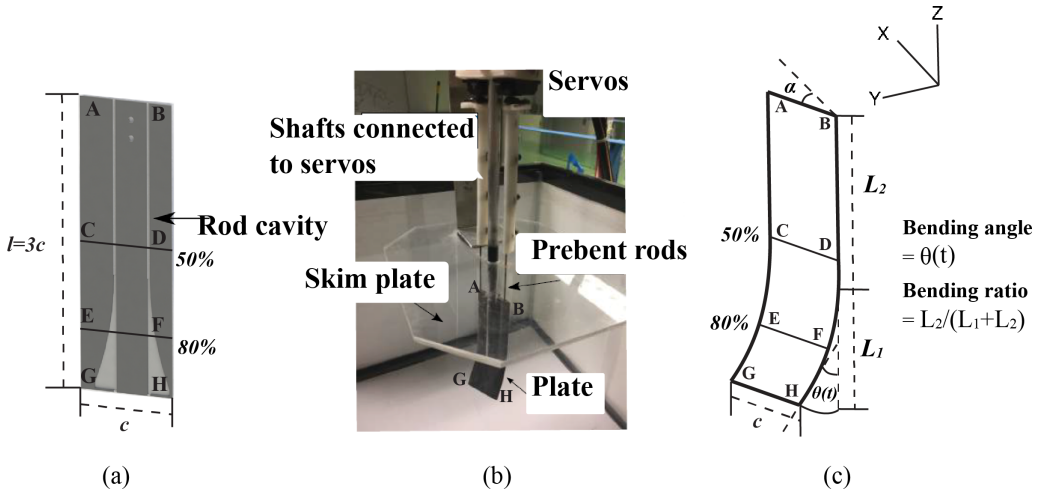


FIG. 1. The construction of the morphing plate: (a) grooves inside a 3D printed plate for holding prebent rods; (b) the plate-rod assembly is connected to servos, which bend the plate along the span; (c) the definition of bending angle and bending ratio. The tips are marked by AB and GH; the 50% span and the 80% span are, respectively, marked by CD and EF.

increasing tip deflection per degree of rotation. The rods were rotated with the help of two servos [Fig. 1(b)] with logic provided by a microcontroller.

The plate was designed to have a bending ratio of 0.65 and a maximum bending angle of 30° . The bending ratio is defined as the ratio of the plate's bent length to the total span [Fig. 1(c)]. The bending angle is defined as the angle between the horizontal and the tip tangent [Fig. 1(c)]. A bending rate t_{bend} of 1 s was implemented by programming the servos. To measure the bending rate, we marked some visible dots at the plate's leading edge and captured the video images of the plate's dynamic bending. Later, individual frames were extracted and the dots' movement was analyzed to obtain the time displacements of individual dots along the span. This information was later used to reconstruct the plate deformation in the immersed boundary method applied in the direct numerical simulation (DNS).

The flat-plate wing was held at a constant angle of attack (α) of 30° . During all the tests reported in this paper, the wing was started from rest with an acceleration of 0.1 m/s^2 and it reached the final towing velocity 0.05 m/s in 0.5 s (t_{ac}). The Reynolds number (Re), based on the chord and this final towing velocity, was 2400. As the wing was accelerated from rest, the wing was bent dynamically for 1 s away from the towing direction. The nondimensional time t^* was calculated by dividing time (t) with t_{ac} . Hence, bending was completed at $t^* = 2$, while the plate completed acceleration at $t^* = 1$ (Fig. 2).

B. Towing tank and imaging system

The flat plate was towed in a fish tank having a length of 1 m and a cross section of $0.45 \times 0.45 \text{ m}$ (Fig. 3). It was fitted with a traverse system (Velmex bi-slide) for towing the models in water. The traversing slide's speed and acceleration were tracked by an ultrasonic motion sensor (PASCO PS-2103A3).

We measured the flow field of the wing with the help of planar particle image velocimetry (PIV). The flow was seeded with silver-coated hollow glass spheres of diameter $13 \mu\text{m}$ (Potter industries). Then, the flow field was illuminated by a continuous-wave green laser (Dragonlaser) with a power of 2 W. A high-speed camera (AOS-SPRI), whose resolution is 1280×1024 pixels and frame rate is 500 fps, captured the images recording the flow field's changes. The output from the laser head

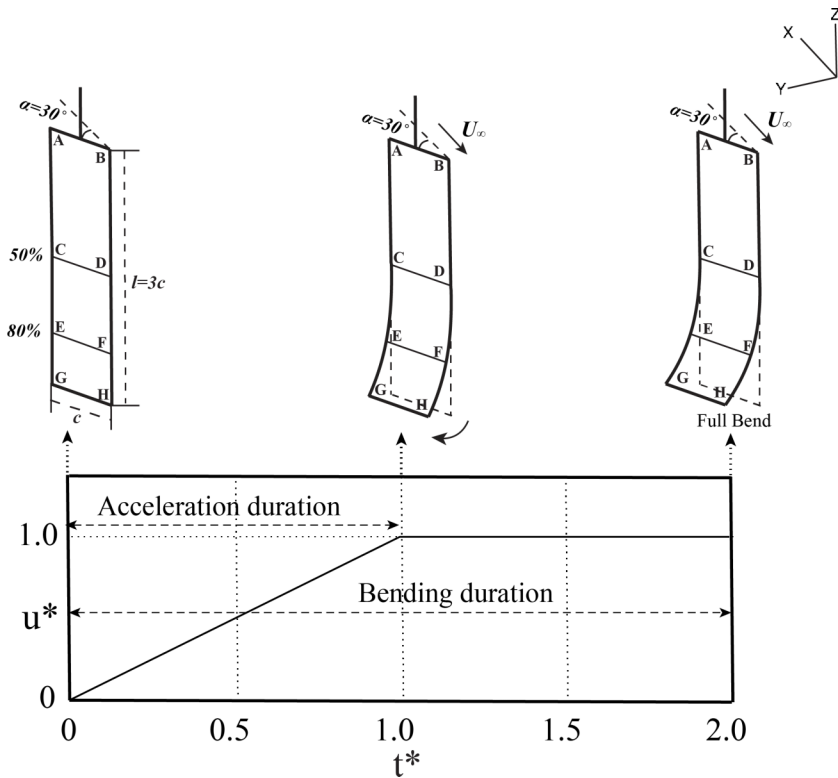


FIG. 2. The kinematics of the plate motion. The plate is accelerated for $t^* = 1$ and the bending is completed at $t^* = 2$. u^* is obtained by normalizing u (velocity) by U_∞ (0.05 m/s).

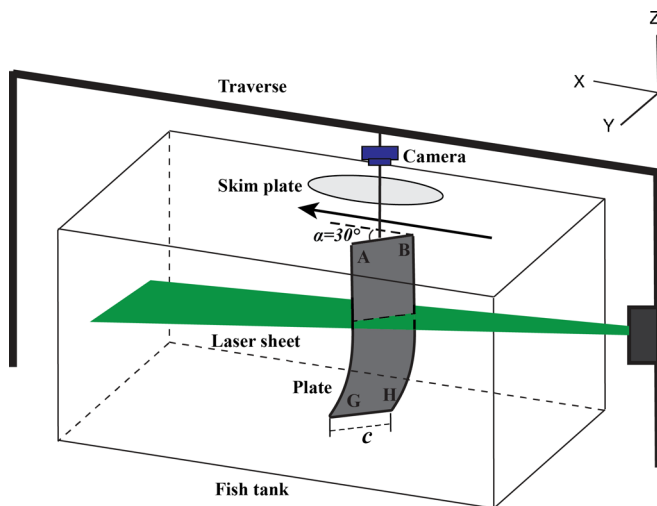


FIG. 3. Experimental setup: a 1-m-long towing tank facility equipped with Velmex traverse. The camera travels along with the plate. A skim plate is used to prevent the formation of surface waves during towing. PIV measurements were conducted at 50% and 80% span of the plate (CD and EF in Fig. 1).

consists of a beam with a diameter of 2 mm, which was expanded into a thin sheet of 1 mm thickness using a cylindrical and a spherical lens. The data were processed using PIVLAB, a MATLAB-based software [18]. During the postprocessing of the PIV data, a multipass iteration scheme was used. The first pass involved a window size of 32×32 pixels and with 50% overlap, followed by three passes with window size 16×16 pixels and with 50% overlap. Further postprocessing of the data was performed using MATLAB.

C. Governing equations

The flow is described by the nondimensionalized incompressible Navier-Stokes equations,

$$\nabla \cdot \mathbf{u} = 0, \quad \frac{\partial \mathbf{u}}{\partial t} + \mathbf{u} \cdot \nabla \mathbf{u} = -\nabla p + \frac{1}{\text{Re}} \nabla^2 \mathbf{u} \quad \text{in } \Omega, \quad (1)$$

$$\mathbf{u} = \mathbf{V} \quad \text{on } S, \quad \mathbf{u} = 0 \quad \text{on } \Gamma_\infty, \quad \frac{\partial p}{\partial n} = 0 \quad \text{on } \Gamma_\infty, \quad (2)$$

where Ω stands for the fluid domain, S and Γ_∞ represent the solid boundary and the far-field boundary, and n is the unit normal vector at the Γ_∞ . \mathbf{u} is the flow velocity and \mathbf{V} is the velocity vector at the boundary. The Reynolds number is defined as $\text{Re} = \frac{U_\infty c}{\nu}$ based on the free stream velocity U_∞ and the chordwise length c .

D. Numerical algorithm

The flexible plate accelerating in the fluid is a typical complex moving boundary fluid-structure interaction (FSI) problem, which is still challenging for the numerical simulation. The immersed boundary method (IBM), proposed by Peskin [19], has proved its excellent ability to handle the complex motion or metabolic solid shape problems in FSI [20–24]. Its innovative procedure utilizes two sets of independent grids: a fixed Eulerian grid for the fluid flow and a moving Lagrangian grid for the immersed boundary. A simple interpolation rule transfers the information between two sets of meshes. Simultaneously, this method considers the effects of the solid on the fluid as an external force term in the fluid governing equations and solves these equations over the entire computational domain. Its most distinct advantage is avoiding the grid's requirement to conform to the complex geometrical structure of the solid [25].

A staggered Cartesian mesh with stretching functions as local refinement is utilized in our simulation due to its benefits of computational efficiency and numerical stability. For the spatial discretization and the time advancement, we chose the second-order central difference scheme and the third-order Runge-Kutta and Crank-Nicolson scheme separately. At the same time, a typical projection method for incompressible flow conditions is applied. The time step is limited by the Courant-Friedrichs-Lewy (CFL) constraint [26–28].

E. Computational setup

The dimensions of the flat plate in our simulation are shown in Fig. 4(b) with a chord length of c , a span length of $l = 3c$, and a thickness of $h = 0.08c$. The angle of attack is 30° . The size of the computational domain is $12c \times 4c \times 5c$, and the mesh along the x direction is stretched to improve the computation efficiency in which the length of the uniform part is $5.8c$. A corresponding stretched Cartesian mesh is used for an overall Eulerian description of the combined fluid and the solid domain with a size of $600 \times 400 \times 500$, as shown in Fig. 4(a). The grid is clustered near the solid region with a minimum size of $\Delta x = \Delta y = \Delta z = 0.01$.

The chord length (c) and the free stream speed (U_∞) are chosen as the characteristic length and the characteristic speed, respectively. In the simulation, the Reynolds number is defined as $\text{Re} = \frac{U_\infty c}{\nu}$ based on the free stream velocity and the chordwise length c . All the nondimensional values of the experimental parameters used in the simulation are shown in Table I.

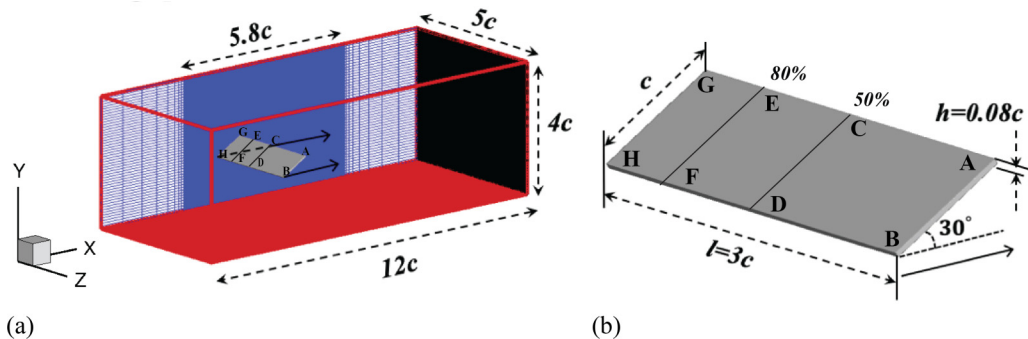


FIG. 4. Schematics of (a) the computational domain and Cartesian mesh employed in the current simulation. The mesh along the x direction is stretched and the length of the uniform part is $5.8c$; (b) the dimensions of the plate used in the current study. The solid arrow stands for the moving direction of the plate, which is along the x -axis direction.

F. Analytical model

We modified an analytical model, originally developed by Wong *et al.* [29], by altering the expression of the effective leading-edge velocity, where we factored in the bending velocity of the plate. Here we first describe the salient features of Wong *et al.*'s [29] original model before describing our modification. In the original model, the LEV, represented by a semicylindrical region, gradually grows in size due to the mass flow brought in by the shear layer. This shear layer is assumed to be of a fixed thickness d [Fig. 5(a)]. The outer shear layer velocity $u(d, t)$ is assumed to be the sum of three separate velocity components, namely,

$$u(d, t) = u_b + u_i + u_k, \quad (3)$$

where u_b is the component of velocity caused by the speeding up of the flow over the semicylindrical blockage, u_i is the induced velocity from the vortex itself, and, finally, u_k is the component of the effective leading-edge velocity u_e along the direction of shear layer velocity. The three velocities are computed as

$$u_b = U_\infty \left[1 + \frac{R^2(t)}{r^2} \right] \sin(\alpha_e), \quad (4)$$

$$u_i = \frac{\Gamma(t)}{2\pi r}, \quad (5)$$

$$u_k = u_e \sin(\alpha_e). \quad (6)$$

TABLE I. Nondimensional parameter space.

| Variable | Dimensional value | Nondimensional value |
|----------------------------------|----------------------|----------------------|
| Plate chord (c) | 0.05 m | 1 |
| Plate span (l) | 0.15 m | 3 |
| Accelerating time (t_{ac}) | 0.5 s | 0.5 |
| Acceleration (a_1) | 0.1 m/s ² | 2 |
| Free stream speed (U_∞) | 0.05 m/s | 1 |
| Angle of attack (α) | 30° | |
| Aspect ratio (AR) | | 3 |
| Bending ratio (BR) | | 0.65 |
| Reynolds number (Re) | | 2400 |

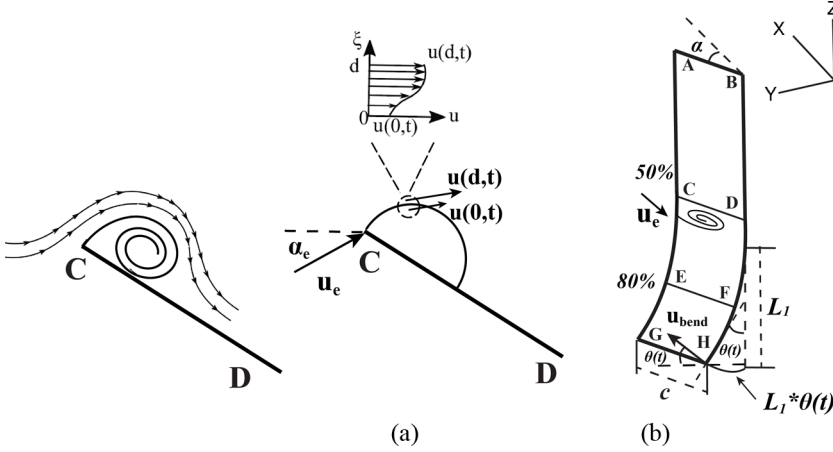


FIG. 5. Details of the analytical model: (a) The LEV is modeled as a semicylindrical blockage in Wong *et al.* [29], where vorticity is being supplied by a shear layer; (b) the modification implemented in the analytical model in the present work, where the component of the bending velocity was subtracted from the effective velocity on the leading edge.

Here, $R(t)$ is the radius of the semicylindrical blockage and r is the distance of the outer shear layer from the center of the semicircle, i.e., $r = R(t) + d$. α_e is the effective angle of attack and $\Gamma(t)$ is the circulation of the LEV. In this formulation, we disregard wake vorticity and the bound vortex of the flat plate itself. In fact, Ford and Babinsky [30] have shown that the bound circulation on an accelerating wing is negligible and the LEV contributes most of the lift.

Next, we calculate the mass flow rate into the LEV brought in by the shear layer as

$$\dot{m}(t) = \rho \int_0^{t_1} \left[\frac{u(0,t) + u(d,t)}{2} \right] dt, \quad (7)$$

followed by the calculation of the radius of the vortex as

$$R(t) = 2 \sqrt{\frac{2 \dot{m}(t)}{\pi \rho}}. \quad (8)$$

The final step is to calculate the circulation as

$$\Gamma(t) = \oint u dl = \pi u(d,t) R(t). \quad (9)$$

To calculate $\Gamma(t)$, we start with an initial \dot{m} at $t = 0$ using Eq. (3), where $R(t)$ is assumed to be zero at the first time step. After calculating \dot{m} at $t = 0$, we update $R(t)$ in subsequent time steps using Eq. (8) and calculate circulation $\Gamma(t)$, using Eq. (9). Equations (3) to (9) have been taken from Wong *et al.* [29].

To calculate the circulation growth on the part of the wing that is being bent, at every time step, we modify u_k by subtracting the component of the bending velocity u_{bend} from u_k [Fig. 5(b)]. Here, we assume a constant bending velocity, given by

$$u_{bend} = \frac{L_1 * \theta}{t_{bend}}, \quad (10)$$

where $\theta = 30^\circ$, $L_1 = 0.35 * \text{span}$, and $t_{bend} = 1$ s in the present case. Then, at every time step, we subtract the horizontal component of u_{bend} and write

$$u'_e(t) = u_e(t) - u_{bend} * \cos[\theta(t)]. \quad (11)$$

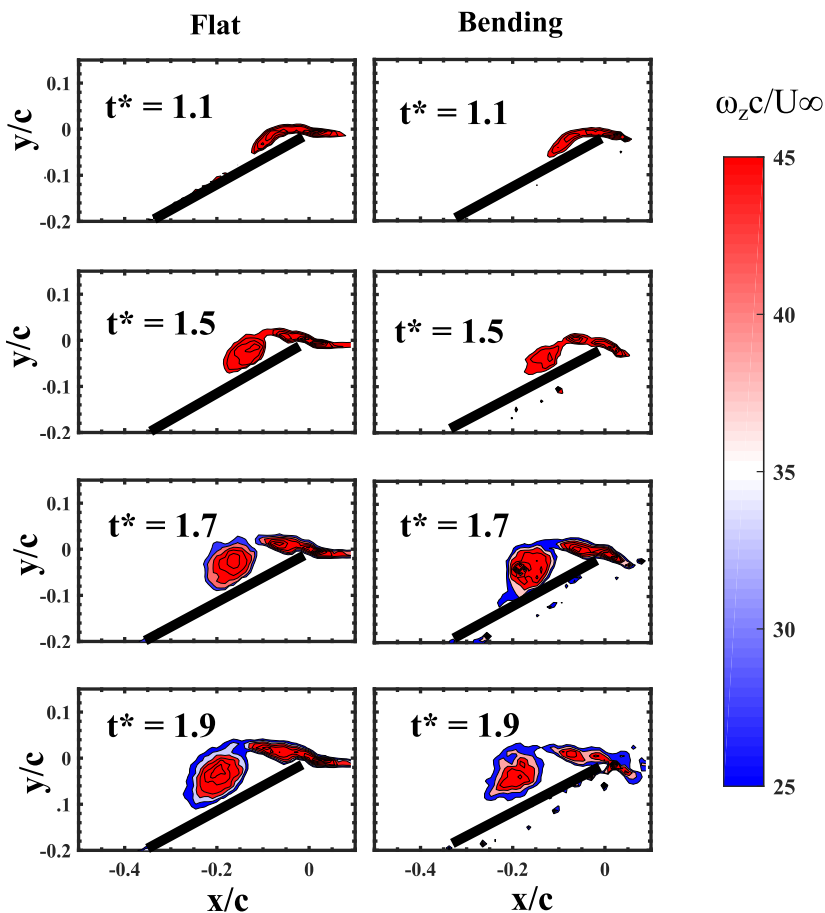


FIG. 6. The development of the LEV on the midspan CD (50% span) of the plate from PIV measurements: when no bending was applied (left column) and when bending was applied (right column). The contour plots are created from normalized spanwise vorticity. The cutoffs were selected at each t^* to exclude the boundary layer.

Finally, we use this u'_e in Eq. (6) to calculate u_k .

G. Vorticity transportation

To account for the three-dimensional effect—such as the vorticity convection along the spanwise direction—we need to consider the vorticity transport equation. This equation for an incompressible fluid is

$$\frac{\partial \boldsymbol{\omega}}{\partial t} + (\mathbf{u} \cdot \nabla) \boldsymbol{\omega} = (\boldsymbol{\omega} \cdot \nabla) \mathbf{u} + \nu \nabla^2 \boldsymbol{\omega}, \quad (12)$$

where $\mathbf{u} = [u, v, w]$ is the velocity field and $\boldsymbol{\omega} = [\omega_x, \omega_y, \omega_z]$ is the vorticity vector. In this paper, we focus on the spanwise (ω_z) component of the vorticity transport equation, which is given by the following equation (neglecting the effects of viscous diffusion):

$$\frac{\partial \omega_z}{\partial t} + u \frac{\partial \omega_z}{\partial x} + v \frac{\partial \omega_z}{\partial y} + w \frac{\partial \omega_z}{\partial z} = \omega_x \frac{\partial w}{\partial x} + \omega_y \frac{\partial w}{\partial y} + \omega_z \frac{\partial w}{\partial z}, \quad (13)$$

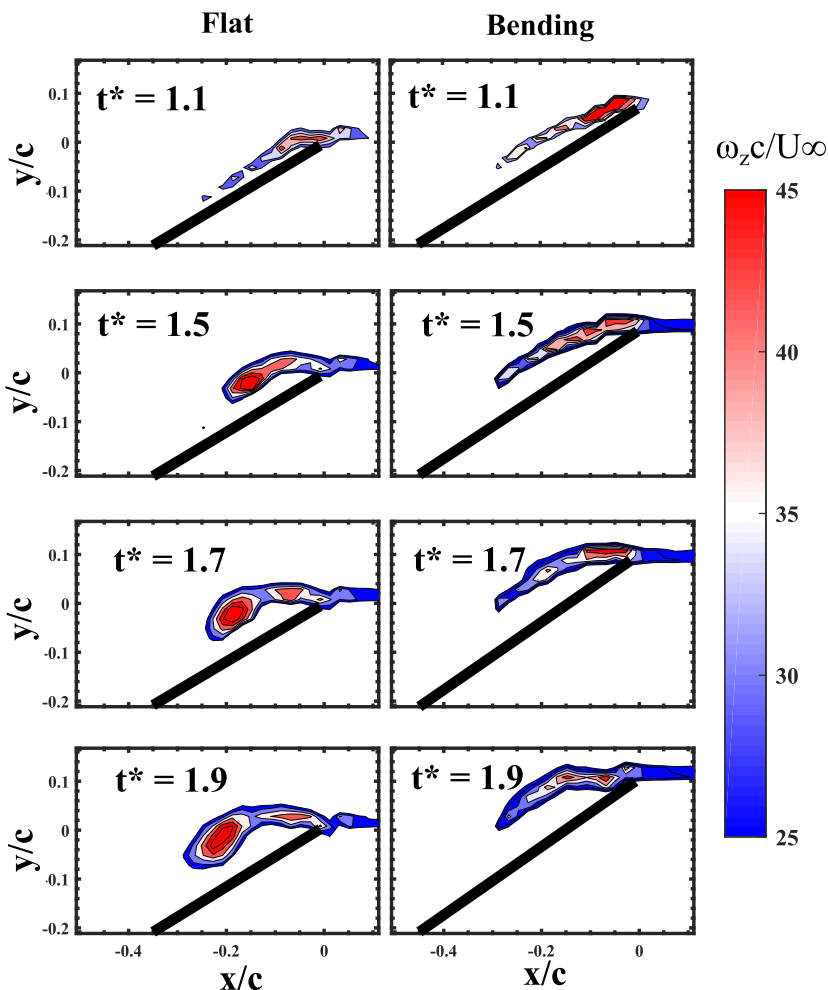


FIG. 7. The development of the LEV on EF (80% span) of the plate from PIV measurements: when no bending was applied (left column) and when bending was applied (right column). The contour plots are created from normalized spanwise vorticity. When the plate was dynamically bent, the growth of the LEV at 80% span was delayed.

where $\frac{\partial \omega_z}{\partial t}$ stands for the temporal rate of change of ω_z ; $u \frac{\partial \omega_z}{\partial x}$, $v \frac{\partial \omega_z}{\partial y}$, and $w \frac{\partial \omega_z}{\partial z}$ represent the convection of ω_z in the streamwise (x), wall-normal (y), and spanwise (z) directions, respectively; $\omega_x \frac{\partial w}{\partial x}$ and $\omega_y \frac{\partial w}{\partial y}$ denote the vortex tilting along the streamwise (x) and the wall-normal (y) directions, and $\omega_z \frac{\partial w}{\partial z}$ denotes vortex stretching.

III. RESULTS AND DISCUSSION

A. The growth of the LEV during bending

The growth of the LEV at the plate's midspan location, during the acceleration phase, is shown in Fig. 6 for both the no-bending and bending cases. These plots show the contours of normalized vorticity—obtained from the PIV experiments—representing the cross section of the LEV at the 50% span of the plate. The cutoff vorticity was selected such that the contours excluded the plate

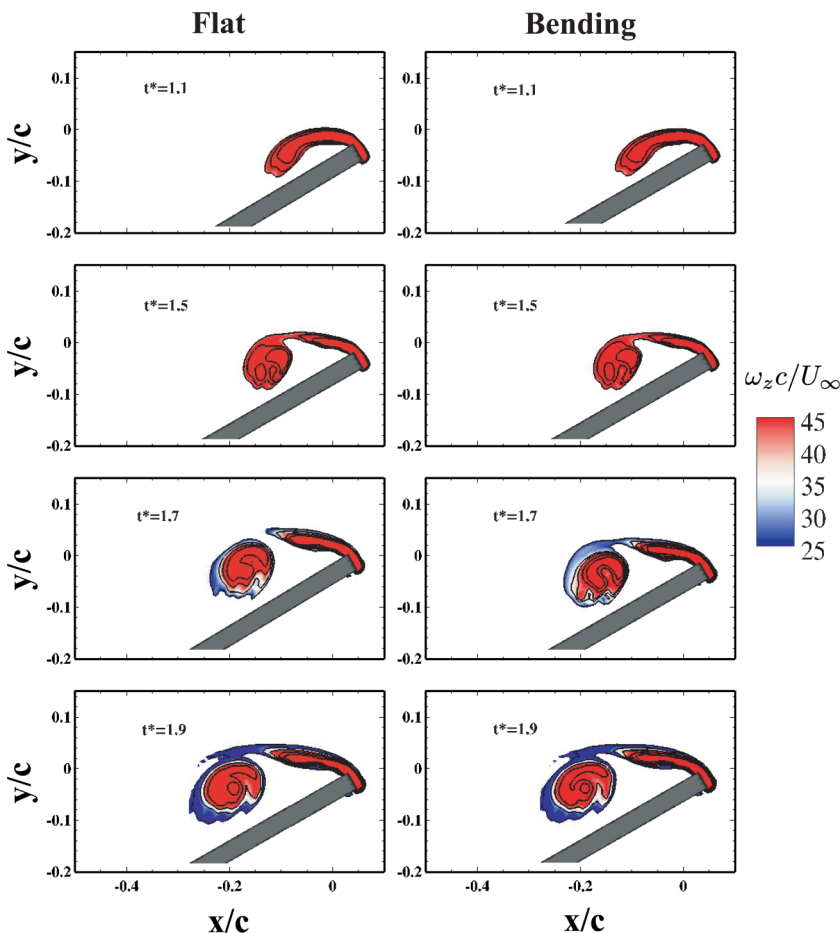


FIG. 8. The LEV development on CD (50% span) of the plate from DNS: when no bending was applied (left column) and when bending was applied (right column).

boundary layer, and these cutoffs were maintained the same for the bending and no-bending cases. It is evident that the LEV was not fully developed at the instant the acceleration was completed (denoted by a $t^* = 1$). In the flat (no-bending) case, the LEV continued to grow up to $t^* = 1.9$. The growth of the LEV at the midspan location was very similar when the plate was subjected to dynamic bending in addition to being accelerated from rest. These contour plots show that the bending action did not influence the growth of the LEV substantially at the midspan.

However, quite dissimilar growth of the LEV was observed when we compared the contour plots of normalized vorticity obtained at 80% span from the PIV experiments. Figure 7 shows that the development of the LEV was significantly delayed when the plate was bent away from the flow dynamically. It is to be noted that this span location was situated in the flexing part of the plate.

Figure 8 shows the simulation results presenting the LEV development at the 50% span. At the 50% span, the vortex shapes of the LEV are almost the same for the flat and bending cases at each moment. Hence, DNS also showed that the bending action did not influence the flow in the midspan region of the plate. In the midspan position where the effects of the vorticity convection are negligible, as shown in Fig. 11, the vortex shapes of the LEV should be similar, even the same. The details about the vorticity convection will be discussed in the next section.

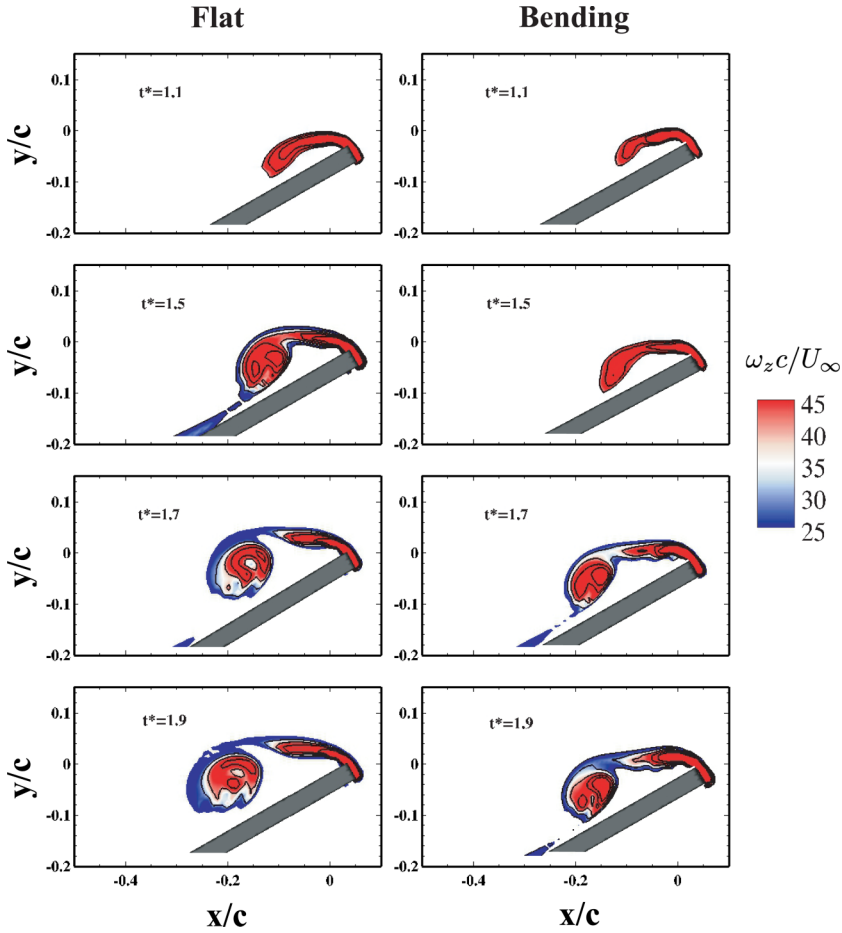


FIG. 9. The LEV development on EF (80% span) of the plate from DNS: when no bending was applied (left column) and when bending was applied (right column).

Figure 9 shows the growth of the LEV at the 80% span of the two cases obtained from DNS. Compared to the flat case, the LEV development in the bending case is significantly delayed, especially at $t^* = 1.5$ and 1.7 . We note some differences between the DNS results and the experimental results at the 80% span at $t^* = 1.9$. We ascribe this difference to three-dimensional effects near the tip where the LEV is strongly affected by the tip vortices.

Next, we compare the variation of the nondimensional circulation of the LEV with t^* , obtained from the analytical model, with that of the experiment and DNS study. To compute the circulation growth from the analytical model, Eqs. (3) to (9) were used for the midspan location, as this part of the span did not experience any bending. For the bent part, we computed the circulation by adding Eqs. (10) and (11). For the experimental and DNS data, the circulation inside the LEV was calculated by integrating the vorticity values inside the outermost contours. The vorticity levels were chosen such that they exclude the boundary layer on the plate. Our aim was to characterize the circulation growth only in the LEV. Hence we did not calculate the circulation growth over the whole plate. Figure 10 shows the result of this comparison. We note that the circulation results of the bending and no-bending cases at 50% span matched well between the analytical, experimental, and DNS results (Fig. 10). This again corroborates the fact that spanwise bending did not influence the flow at the midspan of the plate. However, the circulation growth computed from DNS and

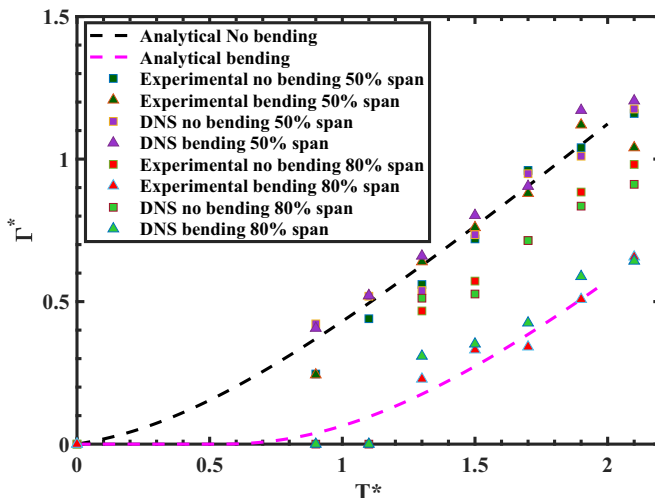


FIG. 10. Comparison of the temporal growth of LEV circulation computed from the analytical model, PIV experiment, and DNS study.

experiment at 80% span for the no-bending case did not match the analytical model. Now, this model does not account for any three-dimensional flow. Since our plate is finite span, we expect that the circulation at 80% span of the plate will not be similar to that of the midspan. We made no attempt to modify the analytical model to account for this finite-span effect, as our focus was the bending part. For the case when the plate was being bent, we incorporated the bending velocity and updated the shear layer velocity, as described in Sec. II F. The circulation growth in the bent part matched well between the analytical model and the experiments and DNS.

We note that we did not present any analytical result for the no-bending case at the 80% span, which we did for the bending case. In fact, we did not attempt to develop a complicated three-dimensional analytical model that takes into account the spanwise vorticity convection. Development of such a model would require detailed treatment of the finite wing effect, which is beyond the scope of our present work. A major aspect of the finite wing effect is the consideration of the downwash caused by the tip vortex. Our present analytical model does not make any such attempt to model the downwash.

B. Effect of bending on the convection of vorticity

This section discusses how the profile bending modifies the vorticity convection inside the LEV by using the DNS data. The comparison of the spanwise vorticity convection flux through the LEV cores of the flat and bending cases in a global view is shown in Fig. 11(a). At the right tips in the two cases, where the plates are not deformed, the two cases' vorticity convection flux is almost the same: the positive flux (red) and the negative flux (blue) are mixed in a chaotic state. For the flat case, the spanwise distribution of the vorticity convection flux is symmetric about the midchord line (50% span). However, for the bending case, the positive vorticity convection flux occupies the entire bent part and plays a dominant role, as shown in Fig. 11(b). The positive vorticity convection is the primary mechanism that delays the growth of the LEV in the deformed area. In the middle of the plate, the effects of the vorticity convection are negligible for both the flat and the bending cases, which explains the similarity of vorticity contours at 50% span.

The spanwise distribution of vorticity convection changing with time t^* is shown in Fig. 12. The vorticity convection gets enhanced with time for both cases. For the flat case, the spanwise vorticity convection mostly occurs near the tips and is always mixed. For the bending case, there is

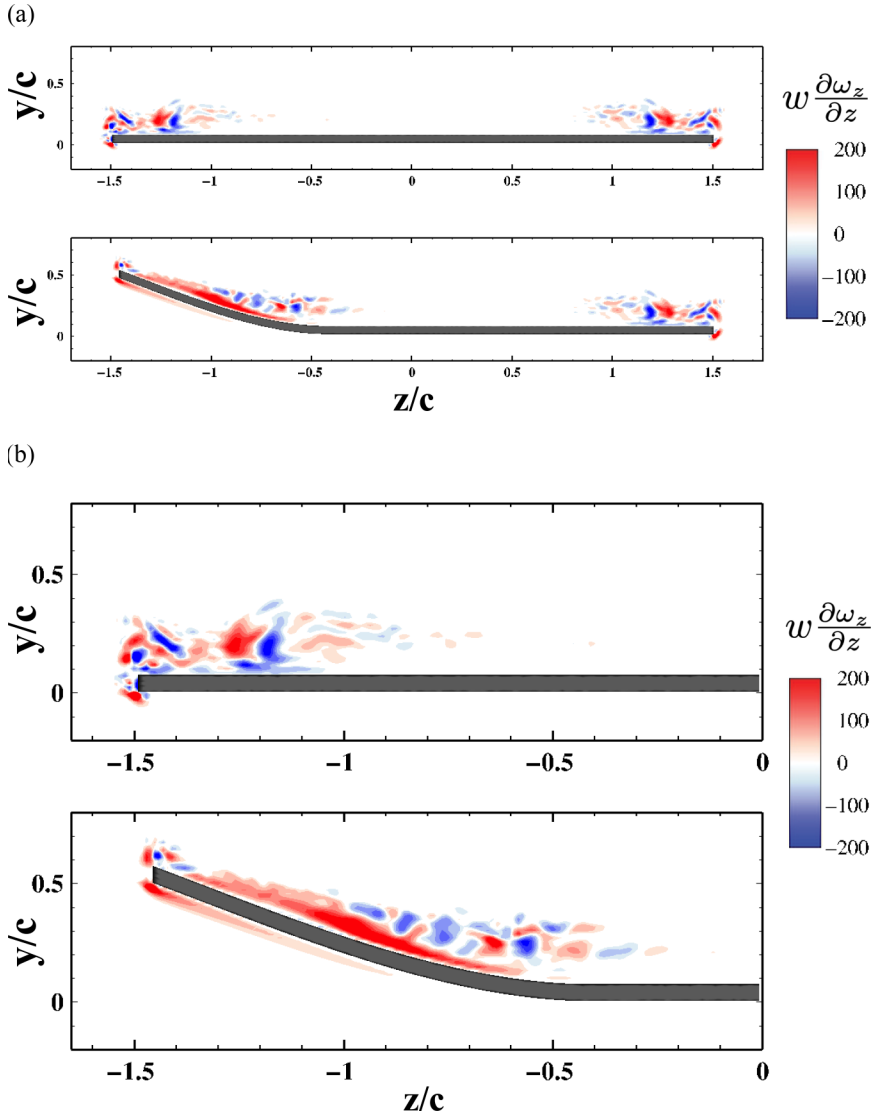


FIG. 11. The comparison of the spanwise vorticity convection flux through the LEV cores of the flat and bending cases in (a) a global view and (b) a zoomed view when $t^* = 1.9$.

always a long and narrow strip of the positive value along the bent part of the plate. These findings conclusively prove that the bending alters the distribution of the vorticity convection flux along the span.

Figure 13 shows the spatial correlation of the LEV (solid black lines), the secondary vortex (dashed black lines), and the vorticity convection flux (colored lines) at 80% spanwise position when $t^* = 1.5$ and 1.9 . For the flat case, when $t^* = 1.5$, the positive vorticity convection flux occupies the upper part of the LEV. Meanwhile, the negative vorticity convection flux dominates the secondary vortex and the boundary between vortices. When $t^* = 1.9$, the secondary vortex rolls up and erodes the connection between the LEV and the leading-edge shear layer, which prompts the LEV to be unstable. For the bending case, when $t^* = 1.5$, the positive vorticity convection dominates the area of the secondary vortex, the boundary between the LEV and the secondary vortex, and part of the

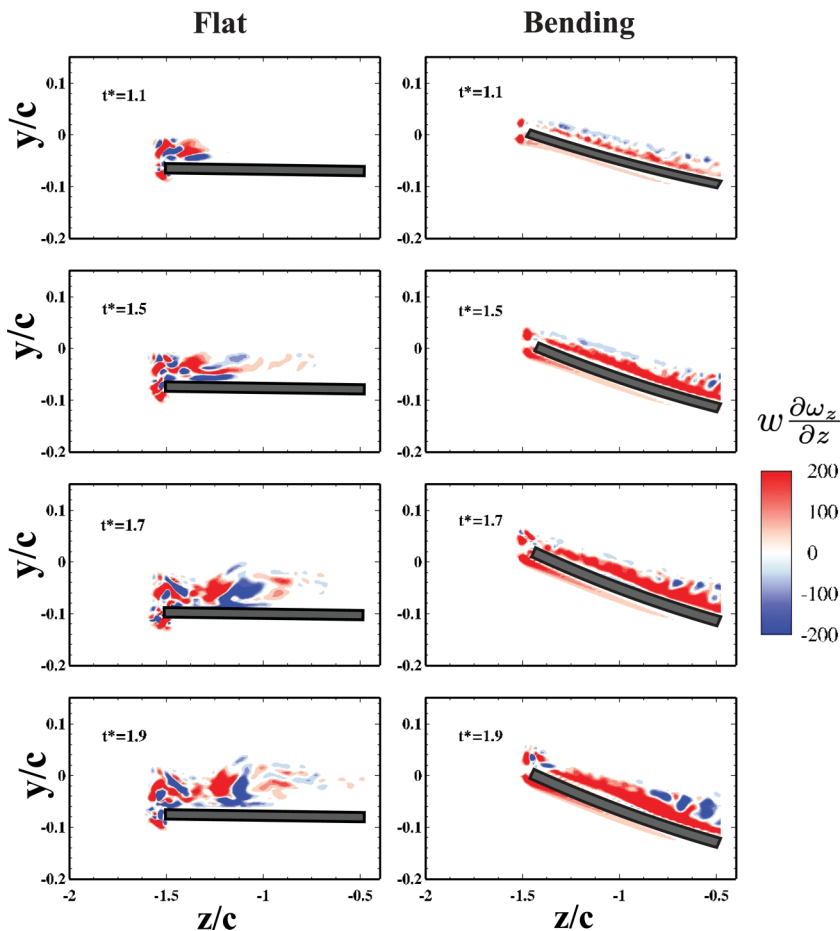


FIG. 12. The comparison of the spanwise vorticity convection flux of the flat (left) and bending (right) cases at different moments in a zoomed view from DNS.

LEV. When $t^* = 1.9$, the positive vorticity convection becomes dominating at the secondary vortex, the boundary, and most of the LEV core. Compared with the flat case, the bending suppresses the development of the secondary vortex and delays the growth of the LEV.

IV. DISCUSSION

The above results show that the bending delays the development of the LEV on a plate whose tip is bending away from the direction of the flow. However, we argue that the main mechanism at play here is the varying shear layer velocity along the leading edge in the bending case. This variation is an outcome of the relative velocity between the plate leading edge and the incoming flow. As the plate's tip moves away from the incoming flow, the shear layer velocity along the leading edge reduces compared to the flat case. Due to this, lesser vorticity is supplied into the LEV and, as a result, its growth gets delayed. This very fact was utilized in the analytical model presented here.

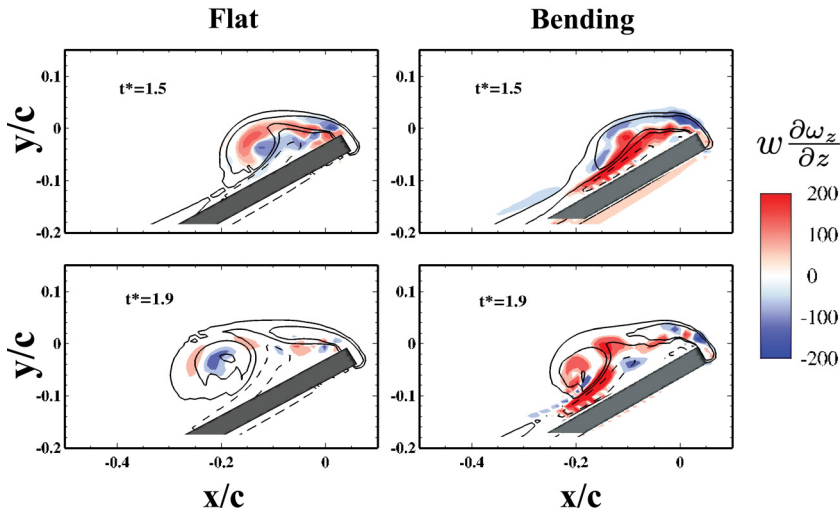


FIG. 13. The vorticity contours and the vorticity convection flux at EF (80% span) when $t^* = 1.5$ (top) and $t^* = 1.9$ (bottom). The solid lines and dashed lines represent the LEV and the secondary vortex, respectively. The vorticity convection flux is colored.

V. CONCLUSION

We investigated the effects of bending on the growth of the LEV on a flat plate which was accelerated from rest to a Reynolds number of 2400. As the plate accelerated, a part of its span was bent away from the flow. We showed experimentally, analytically, and also through DNS that the action of bending delays the growth of the LEV. The DNS results showed that bending modifies the vorticity convection flux along the plate's bent part, resulting from varying shear layer velocity along the leading edge. The bending action creates a relative velocity between the plate and the incoming flow, which changes the shear layer velocity. Since the formation of the LEV on an accelerating plate depends on the vorticity-containing mass brought in by the leading-edge shear layer, a reduced shear layer velocity will delay the growth of the LEV. The DNS results also showed that bending reduces the secondary vorticity that plays a crucial role in the pinch-off of the LEV.

-
- [1] K. N. Lucas, N. Johnson, W. T. Beaulieu, E. Cathcart, G. Tirrell, S. P. Colin, B. J. Gemmill, J. O. Dabiri, and J. H. Costello, Bending rules for animal propulsion, *Nat. Commun.* **5**, 3293 (2014).
 - [2] M. H. Dickinson and K. G. Gotz, Unsteady aerodynamic performance of model wings at low Reynolds numbers, *J. Expt. Biol.* **174**, 45 (1993).
 - [3] J. D. Eldredge and A. R. Jones, Leading-edge vortices: Mechanics and modeling, *Annu. Rev. Fluid Mech.* **51**, 75 (2019).
 - [4] J. O. Dabiri, Optimal vortex formation as a unifying principle in biological propulsion, *Annu. Rev. Fluid Mech.* **41**, 17 (2009).
 - [5] D. Lentink and M. H. Dickinson, Rotational accelerations stabilize leading edge vortices on revolving fly wings, *J. Expt. Biol.* **212**, 2705 (2009).
 - [6] C. P. Ellington, C. Van Den Berg, A. P. Willmott, and A. L. Thomas, Leading-edge vortices in insect flight, *Nature (London)* **384**, 626 (1996).
 - [7] J. G. Wong and D. E. Rival, Determining the relative stability of leading-edge vortices on nominally two-dimensional flapping profiles, *J. Fluid Mech.* **766**, 611 (2015).

- [8] D. E. Rival, J. Kriegerseis, P. Schaub, A. Widmann, and C. Tropea, Characteristic length scales for vortex detachment on plunging profiles with varying leading-edge geometry, *Expt. Fluids* **55**, 1660 (2014).
- [9] D. Kim and M. Gharib, Flexibility effects on vortex formation of translating plates, *J. Fluid Mech.* **677**, 255 (2011).
- [10] C.-K. Kang, H. Aono, C. E. Cesnik, and W. Shyy, Effects of flexibility on the aerodynamic performance of flapping wings, *J. Fluid Mech.* **689**, 32 (2011).
- [11] A. C. DeVoria and M. J. Ringuette, The force and impulse of a flapping plate performing advancing and returning strokes in a quiescent fluid, *Expt. Fluids* **54**, 1515 (2013).
- [12] J.-T. Kim, Y. Jin, and L. P. Chamorro, Dynamics of flexible plates and flow under impulsive oscillation, *J. Fluids Struct.* **87**, 319 (2019).
- [13] P. M. Mancini, A. R. Jones, K. O. Granlund, and M. V. Ol, Unsteady aerodynamic response of a rapidly started flexible wing, *Intl. J. Micro Air Veh.* **7**, 147 (2015).
- [14] R. Wootton, R. Herbert, P. Young, and K. Evans, Approaches to the structural modeling of insect wings, *Philos. Trans. R. Soc. London B* **358**, 1577 (2003).
- [15] S. Heathcote, Z. Wang, and I. Gursul, Effect of spanwise flexibility on flapping wing propulsion, *J. Fluids Struct.* **24**, 183 (2008).
- [16] P. Liu and N. Bose, Propulsive performance from oscillating propulsors with spanwise flexibility, *Proc. Royal Soc. Lond. Ser. A: Math., Phys. Eng. Sci.* **453**, 1763 (1997).
- [17] J. G. Wong and D. E. Rival, Rapid manoeuvring with spanwise-flexible wings, *J. Fluids Struct.* **75**, 1 (2017).
- [18] W. Thielicke and E. Stamhuis, PIVLAB—towards user-friendly, affordable and accurate digital particle image velocimetry in MATLAB, *J. Open Res. Software* **2**, e30 (2014).
- [19] C. S. Peskin, Numerical analysis of blood flow in the heart, *J. Comput. Phys.* **25**, 220 (1977).
- [20] T. Yang, M. Wei, and H. Zhao, Numerical study of flexible flapping wing propulsion, *AIAA J.* **48**, 2909 (2010).
- [21] M. Xu and M. Wei, Using adjoint-based approach to study flapping wings, in *51st AIAA Aerospace Sciences Meeting including the New Horizons Forum and Aerospace Exposition* (AIAA, 2013), p. 839.
- [22] M. Wei and M. Xu, A continuous adjoint-based approach for the optimization of wing flapping, in *32nd AIAA Applied Aerodynamics Conference* (AIAA, 2014), p. 2048.
- [23] M. Xu, M. Wei, C. Li, and H. Dong, Adjoint-based optimization of flapping plates hinged with a trailing-edge flap, *Theor. Appl. Mech. Lett.* **5**, 1 (2015).
- [24] T. Yang, M. Wei, K. Jia, and J. Chen, A monolithic algorithm for the flow simulation of flexible flapping wings, *Intl. J. Micro Air Veh.* **11**, 1756829319846127 (2019).
- [25] M. Cerrolaza, S. Shefelbine, and D. Garzón-Alvarado, *Numerical Methods and Advanced Simulation in Biomechanics and Biological Processes* (Academic Press, Barcelona, Spain, 2017), p. 454.
- [26] M. Xu, M. Wei, T. Yang, and T. Burton, Nonlinear structural response in flexible flapping wings with different density ratio, in *49th AIAA Aerospace Sciences Meeting including the New Horizons Forum and Aerospace Exposition* (AIAA, 2011), p. 376.
- [27] M. Xu and M. Wei, Using adjoint-based optimization to study kinematics and deformation of flapping wings, *J. Fluid Mech.* **799**, 56 (2016).
- [28] M. Xu, M. Wei, C. Li, and H. Dong, Adjoint-based optimization for thrust performance of three-dimensional pitching-rolling plate, *AIAA J.* **57**, 3716 (2019).
- [29] J. G. Wong, J. Kriegerseis, and D. E. Rival, An investigation into vortex growth and stabilization for two-dimensional plunging and flapping plates with varying sweep, *J. Fluids Struct.* **43**, 231 (2013).
- [30] C. P. Ford and H. Babinsky, Lift and the leading-edge vortex, *J. Fluid Mech.* **720**, 280 (2013).